JMEPEG (2022) 31:1667–1678
https://doi.org/10.1007/s11665-021-06292-0


1059-9495/$19.00

# Influence of Electrolyte Compositions and Electrical Parameters on Thermal Properties of Micro-Arc Oxidized AZ91 Alloy

*Ekin Selvi, Faiz Muhaffel, Yakup Yürektürk, Ali Serdar Vanlı, and Murat Baydoğan*

Submitted: 6 April 2021 / Revised: 28 August 2021 / Accepted: 19 September 2021 / Published online: 6 October 2021

**In this study, AZ91 Mg alloy was micro-arc oxidized using different voltages in silicate- and aluminate/phosphate-based (dual) electrolytes that included $K_2ZrF_6$ or $Na_2ZrO_3$ as the Zr source for synthesizing $ZrO_2$ in the micro-arc oxidation (MAO) coatings. Structural characterizations were done by using scanning electron microscopy and x-ray diffraction techniques. MAO coating characteristics of different samples were compared by measuring coating thickness, surface roughness, average pore size, and total pore fraction. Both hardness and pull-off tests were conducted to characterize the mechanical properties of the coatings. Thermal conductivity measurements and thermal shock tests were also carried out to evaluate the effect of the electrolyte composition and the type of Zr containing compound. It was found that the equivalent thermal conductivity of the MAOed samples can be reduced up to 30% compared to the bare AZ91 alloy. The decrease of the thermal conductivity was mainly attributed to formation of a thicker and denser MAO coating, and the incorporation of $ZrO_2$ phase into the fabricated MAO coating. Finally, increased thermal shock resistance was strongly correlated with a lower hardness and higher cohesive strength of the MAO coating, which also leads to smaller crack formation and spallation-free surface characteristics.**

**Keywords** magnesium alloy, micro-arc oxidation, thermal properties, zirconium

## 1. Introduction

Mg alloys have a wide range of applications in the automotive, electronic, and aerospace industries due to their superior properties such as high specific strength and stiffness, low density (mostly about 1.8 g/cm$^3$), good machinability, and high damping capacity (Ref 1-3). Mg alloys are promising substitutes for aluminum alloys because of their advantage in reducing the weight of structural components around 33%, owing to their lower density compared to commercial aluminum alloys (Ref 4). Among various Mg alloys, AZ91 alloy (containing 9 wt.% Al and 1 wt.% Zn) is the most widely used due to their excellent combination of castability, mechanical properties, and corrosion resistance (Ref 5). However, AZ91 alloy has a low high-temperature creep resistance (Ref 6), which restricts its use when high-temperature surface protection is needed. Thus, surface modification is one of the first approaches to enhance the surface properties of commercial Mg alloys. Suitable surface treatments can provide adequate protection against crucial problems related to elevated service temperatures and also ensure an environmentally friendly procedure, which can significantly increase the number of practical applications of Mg-based alloys.

Among many surface modification techniques, the micro-arc oxidation (MAO) process is a multi-factor controlled technique that offers a promising solution to overcome the high-temperature limitations of Mg alloys, as it forms a hard, thick, and well-adherent oxide layers on the surface. Also, characteristics of the MAO coatings can be tailored by regulating the voltage, current density, duty cycle, and frequency, as well as varying the nature of the substrate and electrolyte composition (Ref 3, 7).

The MAO process of Mg alloys is commonly employed in alkaline electrolytes containing $AlO_2^-$, $PO_4^{3-}$, and $SiO_3^{2-}$ ions, which passivate metallic alloys effectively. These ions promote an oxide coating mainly composed of $MgAl_2O_4$, $Mg_3(PO_4)_2$, and $Mg_2SiO_4$ phases according to their reactions with Mg ions arising from the substrate (Ref 7). It has been reported that mixing different inorganic compounds in MAO electrolytes can enhance the properties of MAO coatings, leading to the formation of thicker and denser coating consisting of beneficial complex oxides at the surface of the MAOed alloy, which also promotes strong metal passivation as wear- and corrosion-resistant coatings are formed (Ref 8).

The MAO coating is a hard and chemically stable oxide-based surface layer with a low thermal conductivity, which not only enhances wear and corrosion resistance but also contributes to the thermal insulation of the surface (Ref 9, 10). In particular, zirconia ($ZrO_2$) containing coatings are broadly applied in thermal protection of the metallic alloys exposed to elevated temperatures due to their low thermal conductivity,

**Ekin Selvi**, Department of Metallurgical and Materials Engineering, Istanbul Technical University, 34469 Istanbul, Turkey; and Department of Chemical and Process Engineering, Yalova University, 77200 Yalova, Turkey; **Faiz Muhaffel** and **Murat Baydoğan**, Department of Metallurgical and Materials Engineering, Istanbul Technical University, 34469 Istanbul, Turkey; **Yakup Yürektürk**, Department of Metallurgical and Materials Engineering, Bursa Technical University, 16310 Bursa, Turkey; and **Ali Serdar Vanlı**, Department of Mechanical Engineering, Yıldız Technical University, 34349 Istanbul, Turkey. Contact e-mail: baydogan@itu.edu.tr.

high resistance to thermal shock, and internal oxidation resistance (Ref 11). It was previously reported that electrolytes containing various Zr-based compounds or zirconia particles induced the formation of $ZrO_2$ phase and/or $ZrO_2$ containing complex phases in the generated MAO coatings (Ref 9, 12-14). Zhong et al. (Ref 15) studied the thermal shock behavior of $ZrO_2$ incorporated MAO coatings on the Ti6Al4V alloy using different electrolytes. They found that the MAO coating consisted of $TiO_2$, $ZrO_2$, and $Al_2TiO_5$ phases with a porous microstructure exhibiting significantly higher thermal shock resistance compared to the $SiO_2$ coating formed by the sol–gel method. Wang et al. (Ref 12) fabricated MAO coatings on the Ti6Al4V alloy containing m-$ZrO_2$ and $ZrTiO_4$ phases, and found that the high-temperature oxidation resistance of Ti6Al4V was improved up to ten times after MAO treatment in temperatures between 500°C and 800°C. Li et al. (Ref 13) demonstrated that composite MAO coating containing $ZrO_2$ and $ZrTiO_4$ had a higher thermal oxidation resistance compared to the $ZrO_2$-free MAO coating. Wang et al. (Ref 9) investigated the effect of zirconia sol addition into the electrolyte to enhance the thermal insulation of MAO coating on Al-12Si alloy, and they concluded that high-temperature properties (i.e., thermal insulation and thermal shock resistance) of the fabricated MAO coating were improved with a higher concentration of the zirconia sol in the electrolyte. An oxide-based ceramic coating with a low thermal conductivity produced by the MAO process has also potentiality to enhance the high-temperature resistance of AZ91 Mg alloy. Krit et al. (Ref 16) reported that thermal conductivity of AZ91 alloy was reduced about 5% by the MAO process. Curran and Clyne (Ref 17) found that the measured thermal conductivity of the MAOed AZ91 alloy was at least an order of magnitude lower than that of bulk Mg alloy. Luo et al. (Ref 18) reported that MAO coating formed on AZ91D alloy consisted of $Al_2O_3$, c-$ZrO_2$, t-$ZrO_2$, $Y_2O_3$, and some Mg-based compounds phases (i.e., MgO, $MgF_2$, and $MgAl_2O_4$), exhibited six times higher oxidation resistance, and showed a spallation-free surface appearance after being exposed to 55 thermal cycles.

Although there are several studies concerning the effect of MAO coatings on thermal insulation properties of Mg alloys, there is still lack of information about the effects of single and dual electrolytes, different Zr sources and applied voltages. It is therefore the main objective of this study is to investigate morphological, structural, and thermal properties of AZ91 Mg alloy after being coated by the MAO process in a single ($Na_2SiO_3$) and dual ($NaAlO_2$ and $Na_3PO_4$) electrolytes with $K_2ZrF_6$ or $Na_2ZrO_3$ additions under different applied voltages.

## 2. Experimental Procedure

### 2.1 MAO Process

Disk-shaped AZ91 samples having 12.6 mm diameter and 4 mm thickness were cut from a cylindrical bar, ground with SiC papers up to 2500 grit, and then rinsed with ethanol and distilled water prior to the MAO process. The MAO equipment consists of a bipolar-pulsed DC power supply, stainless steel electrolyte container also serving as the cathode, air stirring system, and an external cooling unit to maintain the electrolyte temperature below 25°C during the process. Sample designation, corresponding electrolyte compositions, electrical conductivity, and pH values of the electrolytes are presented in Table 1. Since the bipolar-pulsed DC power supply is capable of applying positive and negative voltage pulses with their adjustable durations, the applied positive and negative voltage values are also given in Table 1. Positive ($t^+$) and negative ($t^-$) voltage durations with an idle period ($t^{off}$) between them were held constant as 400 $\mu$s, 400 $\mu$s, and 600 $\mu$s, respectively, and the total processing duration was 6 min. After the MAO process, samples were ultrasonically rinsed with ethanol and distilled water and then dried at the room temperature.

### 2.2 Structural Characterization

Microstructure of bare AZ91 Mg alloy was examined with an optical microscope (Leica DM750M) after being prepared by the conventional manner and etched with 2 % Nital. For the MAOed samples, both surface morphology and elemental composition of the coatings were examined using a field-emission scanning electron microscope (SEM, Zeiss Ultra Plus) equipped with an energy-dispersive x-ray spectrometer (EDS). In addition, the cross-sectional morphology of the coatings was examined using an SEM (Hitachi TM-1000) with a backscattered detector. The qualitative phase identification of the bare and the coated alloys were made using an x-ray diffractometer (XRD, GBC MMA 027) using Cu-K$\alpha$ radiation. The samples were scanned over 2$\theta$ angles from 20° to 70° at a scanning speed of 1°/min. Mean surface roughness (Ra) was determined by a profilometer (Veeco Dektak 6M) using a stylus with a 12.5 $\mu$m tip radius. Quantitative measurements of the surface morphology such as average pore size and total pore fraction values were estimated by an image analysis software (Clemex Professional) using corresponding surface SEM micrographs.

### 2.3 Microhardness Measurements and Pull-Off Tests

Microhardness was measured by a microhardness tester (Wilson Tukon 1102) using a Vickers indenter under a load of 25 g. At least ten indentations were made along the cross section of each sample, and the mean values were reported with standard deviations. Pull-off tests were conducted to quantitatively characterize the adhesion/cohesion strength of the coatings. For this purpose, the MAOed samples were attached to a cylindrical block with a diameter of 25 mm using a suitable epoxy-based adhesive bonding agent (Loctite EA9466) and were kept for three days at the room temperature for curing. The pull-off tests were carried out with a universal testing machine (Shimadzu AG-IC) at a constant crosshead speed of 1 mm/min, and the samples were forced to separate from the block. Following the pull-off tests, surface of the samples was examined under a stereo microscope (Leica MZ16 FA) to reveal any defects formed during the test.

### 2.4 Thermal Conductivity and Thermal Shock Tests

In order to calculate thermal conductivity, thermal diffusivity was first determined by the laser flash method (FlashLine 2000) at 200°C in a nitrogen atmosphere. Colloidal graphite was sprayed on the bare and the MAOed samples, and they were dried to allow uniform absorption of the laser pulse afterward. Specific heat capacity was determined by a comparative method, where reference (graphite) and test samples were measured subsequently under the same condition. Density was measured using the Archimedes' method. Density, thermal diffusivity, and specific heat capacity are presented in Table 2.

**Table 1 Sample designation, corresponding electrical parameters, electrolyte compositions, electrical conductivity, and pH values of the electrolytes**

| Sample designation | Positive/negative applied voltages, V | Electrolyte composition | Electrical conductivity, mS/cm | pH |
|---|---|---|---|---|
| A1 | 440/66 | 10 g/l $Na_2SiO_3$, | 26.8 | 12.7 |
| A2 | 480/72 | 5 g/l $K_2ZrF_6$, | | |
| A3 | 520/78 | 2 g/l KOH | | |
| B | 400/60 | 10 g/l $Na_2SiO_3$ | 28.0 | 12.6 |
| B440 | 440/66 | 5 g/l $Na_2ZrO_3$, | | |
| | | 2 g/l KOH | | |
| C | 360/54 | 10 g/l $NaAlO_2$ | 45.2 | 12.6 |
| C400 | 400/60 | 10 g/l $Na_3PO_4$, | | |
| | | 5 g/l $K_2ZrF_6$ | | |
| | | 2 g/l KF | | |
| | | 2 g/l KOH | | |

**Table 2 Density, thermal diffusivity, and specific heat capacity values to calculate thermal conductivity**

| Sample designation | Density, g/cm$^3$ | Thermal diffusivity, cm$^2$/s | Specific heat capacity, J/kg K |
|---|---|---|---|
| Bare | 1.682 | 0.4463 | 763.5574 |
| A1 | 1.715 | 0.4069 | 744.4486 |
| A2 | 1.725 | 0.3985 | 716.1672 |
| A3 | 1.676 | 0.3758 | 716.1672 |
| B | 1.697 | 0.4154 | 749.8473 |
| C | 1.689 | 0.3285 | 700.9915 |

Finally, the thermal conductivity (λ: W/m.K) is calculated with Eq 1 (Ref 4) using measured density (ρ: kg/m$^3$), thermal diffusivity (α: m$^2$/s), and specific heat capacity ($C_p$: J/g.K).

$$\lambda = C_p.\alpha.\rho \quad \text{(Eq 1)}$$

Thermal conductivity of the coating is then calculated with Eq 2 (Ref 10, 17).

$$K_e = \frac{(t_c + H_s)}{\left(\frac{t_c}{K_c}\right) + \left(\frac{H_s}{K_s}\right)} \quad \text{(Eq 2)}$$

where $K_e$ is the equivalent thermal conductivity of the sample (substrate + coating), $H_s$ is the substrate thickness, $t_c$ is the coating thickness, $K_c$ is the thermal conductivity of the coating, and $K_s$ is the thermal conductivity of the substrate. λ value in Eq 1 is also the equivalent thermal conductivity of substrate + coating, and expressed as $K_e$ in Eq 2. By substituting λ in Eq 1 into $K_e$ in Eq 2, thermal conductivity of the coating was calculated by using thicknesses of the substrate and the coating, and thermal conductivity values of the bare substrate.

Thermal shock resistance of the MAOed samples was evaluated by examining their surfaces under SEM to determine if there was any crack formation after thermal shock test. During the thermal shock test, the samples were hold at 500°C for 5 min in an electrical furnace followed by quenching in water at the room temperature. The samples were then dried and placed in the furnace again to repeat the processes. This procedure was repeated 40 times for all MAOed samples to evaluate the thermal shock resistance of the coatings.

## 3. Results and Discussion

### 3.1 Microstructure of the Bare AZ91 Mg Alloy

Optical micrograph and XRD pattern of as-cast AZ91 alloy used in the present study are shown in Fig. 1(a) and (b), respectively. The microstructure is comprised of α-Mg and β-$Mg_{17}Al_{12}$ phases at the grain boundaries (Fig. 1a), the corresponding XRD pattern (Fig. 1b) confirms the present phases observed in the optical micrographs.

### 3.2 Current Density—Time Response

Variation of the current density with processing time during the MAO process of the samples, which were oxidized in various electrical parameters and electrolyte compositions is shown in Fig. 2. At the early stage of the process (up to 50th s), the current density curves of the samples increased linearly. This stage is known as the initial anodic oxidation and is required for reaching the dielectric breakdown of the formed thin oxide film (Ref 19). Comparing the current density-time response of the samples, it can be seen that higher voltage values increased the maximum current density for all samples used in the present study, causing the dielectric breakdown of the passive oxide film.

Following the initial anodic oxidation stage, it was observed that evenly distributed micro-sparks were dramatically ignited at structural defects in the oxide films of the samples when the slope of the curves changed (Ref 20). As the MAO process for the treated samples proceeded, these micro-discharges continue through the formed micro-channels (Ref 20, 21). After the dielectric breakdown of the passive oxide film (occurrence of the first peak), different characteristics of the curves were observed for the treated samples. For example, the curves of the

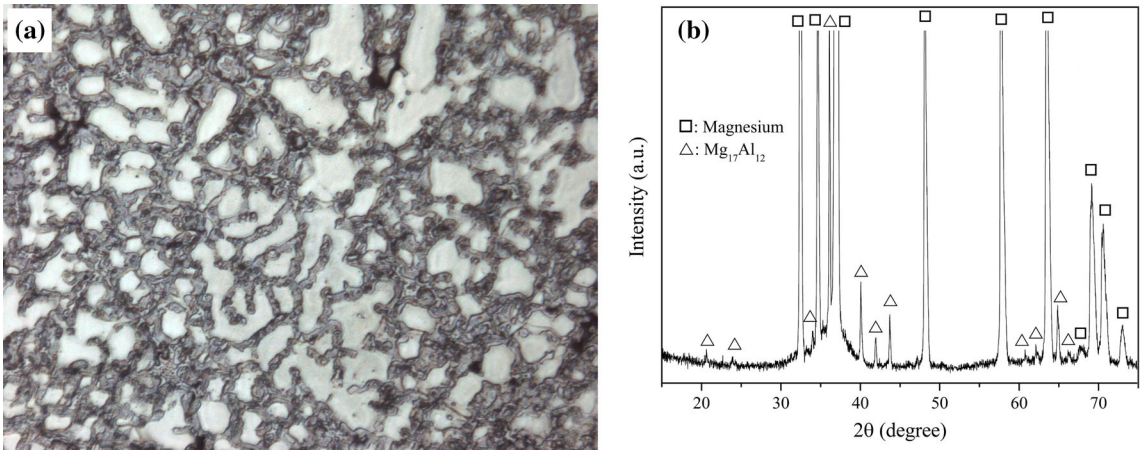


**Fig. 1** (a) Optical micrograph and (b) XRD pattern of the bare AZ91 Mg alloy

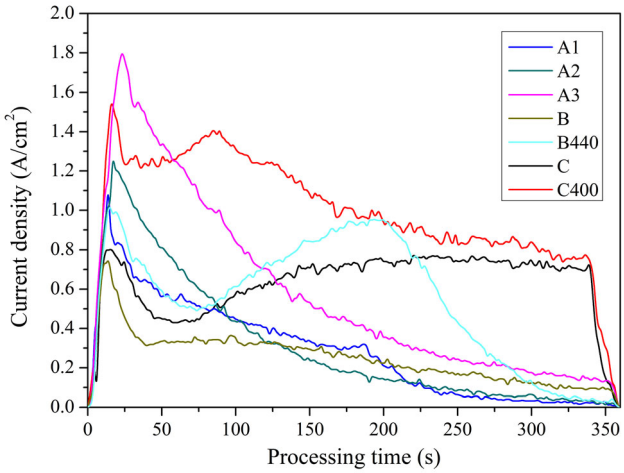


**Fig. 2** Variation of the current density with processing time during the MAO process

samples A1, A2, and A3 showed a continuous reduction in the current density, while the curve exhibited a second peak for the samples B440 and C400 followed by a declining trend up to the end of the process. Variation of the current density for sample B and C was similar in that they exhibited an increment after the peak valley at about 50th. s. However, for sample B, this increment was not significant and the current density continuously decreased afterward, while, for sample C, it was almost constant up to the end of the process, exhibiting more stable variation when compared to those observed for samples B, B440 and C400. This phenomenon can be related to the consistent dissolution and formation of an oxide layer on those samples due to the strong dependence on their electrical parameters and electrolyte compositions (Ref 22). It is worth noting that the sample C and C400, which were oxidized in the electrolyte with the highest electrical conductivity, had the highest current density at the end of the process, even though these samples were oxidized in a relatively lower voltage level than the other samples. This implies that the electrolyte conductivity has a significant effect on the final current density during the MAO process.

Visual appearances of the coating surfaces after the MAO process are shown in Fig. 3. It was shown that the surface appearance can be related with the variation of the current density during the MAO process. In this context, the size and intensity of micro-sparks on the surface have an effect on the visual surface appearance of the samples. For example, the size and intensity of micro-sparks on the surface of samples A1, A2, and A3 increased as the applied voltage increased, and the micro-spark population decreased gradually up to the end of the process by exhibiting the decrement in the current density. As a result, a lower applied voltage produces a smoother surface for samples A1, A2, and A3 as shown in an increasing order in Fig. 3(a) to (c). The visual appearance of those surfaces can also be accompanied with the mean surface roughness given in Table 3. On the other hand, when the occurrence of the second peak takes place during the MAO process as in the case of B, B440, C, and C400 samples, it was seen that the surface quality deteriorated. The highest deterioration was seen in sample B440 (Fig. 3f) where the peak to valley intensity in the current density response was the highest. The surface deterioration was given in an increasing order for samples B, C, and C400 (Fig. 3d, e, and g), and can be related with the final current density of those samples achieved at the end of the process.

### 3.3 SEM Characterization of the Coatings

SEM micrographs of the MAOed samples are shown in Fig. 4, and the corresponding morphological features such as average pore size, total pore fraction, mean surface roughness, and average coating thickness are presented in Table 3. The samples A1, A2, and A3, which were oxidized in the silicate-based electrolyte with $K_2ZrF_6$ addition as the Zr source exhibited micro-pores varying in size between 2 and 6 $\mu$m and hills surroundings these micro-pores (the typical appearance of a MAOed surface). Increasing the applied positive voltage from 440 to 520 V for samples A1, A2, and A3 reduced the pore fraction to obtain a more compact and denser surface morphology (Fig. 4a-c). These pores were formed during the MAO process when the applied voltage exceeds the dielectric voltage of the passive film (Ref 21). At this stage of the MAO process, discharge channels were generated across the existing oxide layer, and melted materials were ejected through the channels onto the surface. Afterward, the ejected molten

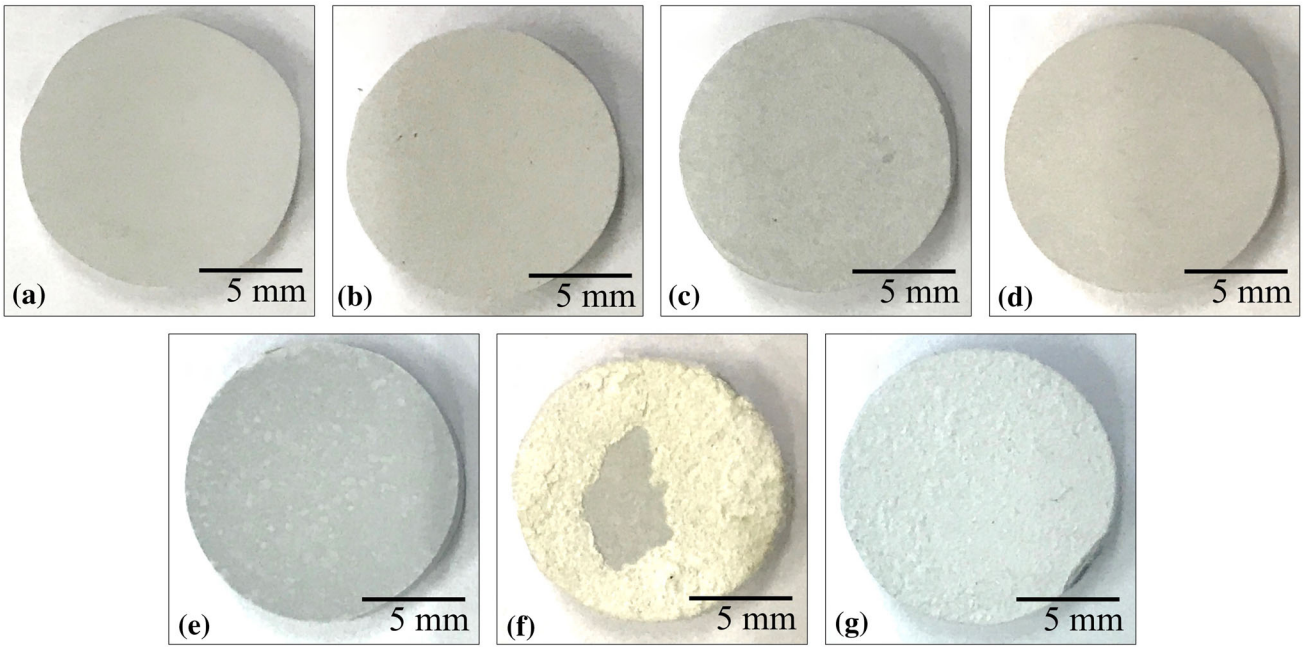


**Fig. 3** Visual appearances of the MAOed samples (a) A1, (b) A2, (c) A3, (d) B, (e) C, (f) B440, and (g) C400

**Table 3 Morphological features of the MAOed samples**

| Sample designation | Average pore size, $\mu$m | Total pore fraction, % | Mean surface roughness, Ra, $\mu$m | Average coating thickness, $\mu$m |
|---|---|---|---|---|
| A1 | 2.32 | 8.8 | 1.80 | 22 |
| A2 | 2.54 | 5.6 | 2.57 | 32 |
| A3 | 5.71 | 2.6 | 6.29 | 61 |
| B | 1.62 | 10.7 | 0.84 | 20 |
| C | 0.96 | 24.8 | 1.13 | 69 |

materials were rapidly cooled by the cold electrolyte surrounding the sample, those channels became visible as the pores on the surface, and thus the ejected materials contributed to the thickening and roughening of the formed oxide layer on the AZ91 alloy. The present results suggest that higher individual discharge density in the micro-pores tended to generate more oxide melts due to violent discharges causing more molten oxide eruption through the pore and, therefore, promoted the formation of higher-altitude craters (Ref 10). When $Na_2ZrO_3$ was added in the silicate-based electrolyte as the zirconium source (Sample B, Fig. 4d), the characteristics of the typical MAO morphology was still preserved. However, a higher number of micro-pores appeared on the surface along with a smaller average pore size, which is probably due to the lowest applied positive voltage during the MAO process. Also, both the average coating thickness and the mean surface roughness of sample B were lower than those of samples A1, A2, and A3. When the MAO process was performed in a dual electrolyte composed of $NaAlO_2$ and $Na_3PO_4$ with the addition of $K_2ZrF_6$ as the Zr source, the surface morphology was significantly altered from the typical appearance of MAOed samples to a highly porous and bone-like structure characterized by higher number of submicron-sized pores interconnecting to each other (Sample C, Fig. 4e). Because the Zr source for sample C was the same as in samples A1, A2, and A3, the observed morphological change was attributed to the dual-component of the electrolyte rather than the Zr source used.

It is also worth mentioning that the electrical conductivity for sample C was higher than the others, promoting fine-spark discharges, the formation of a fine-grain structure and more uniform and smoother coatings (Ref 7, 23). Even though the MAO coating formed by the dual electrolyte was the thickest one when compared to the others as shown in Table 3, it was still relatively smooth. It indicates that the high electrical conductivity of the electrolyte containing $NaAlO_2$ and $Na_3PO_4$ significantly contributed to thickening the coating while keeping the surface smooth during the MAO process. Hence, a thicker, more uniform and smoother coating was produced at the lowest applied voltage (360 V) in the aluminate/phosphate-based electrolyte in which sample C was fabricated.

Elemental composition of the MAO coatings determined by the EDS analysis on their surfaces is presented in Table 4. The content of Mg and oxygen in the coatings was similar in all samples indicating the generation of an MgO phase within the microstructure of MAO coatings. The presence of a high amount of silicon in the MAO coatings formed in silicate-based electrolytes indicates the formation of $Mg_2SiO_4$. Although the contents of the main elements were similar, slight changes occurred due to high-temperature plasma and the quenching effect of the electrolytes (Ref 10). For example, when the Zr content in the MAO coatings was considered, sample B (which was treated in $Na_2ZrO_3$ containing electrolyte) contained the lowest amount of Zr among the MAOed samples. On the other hand, Zr content in sample C was the highest among all samples, even though the applied positive voltage was the lowest for this sample. Although the Zr contents in the coatings of samples A1, A2, and A3 was similar (between 4.03 and 4.51 at.%), sample A3, which was treated at higher applied voltage,

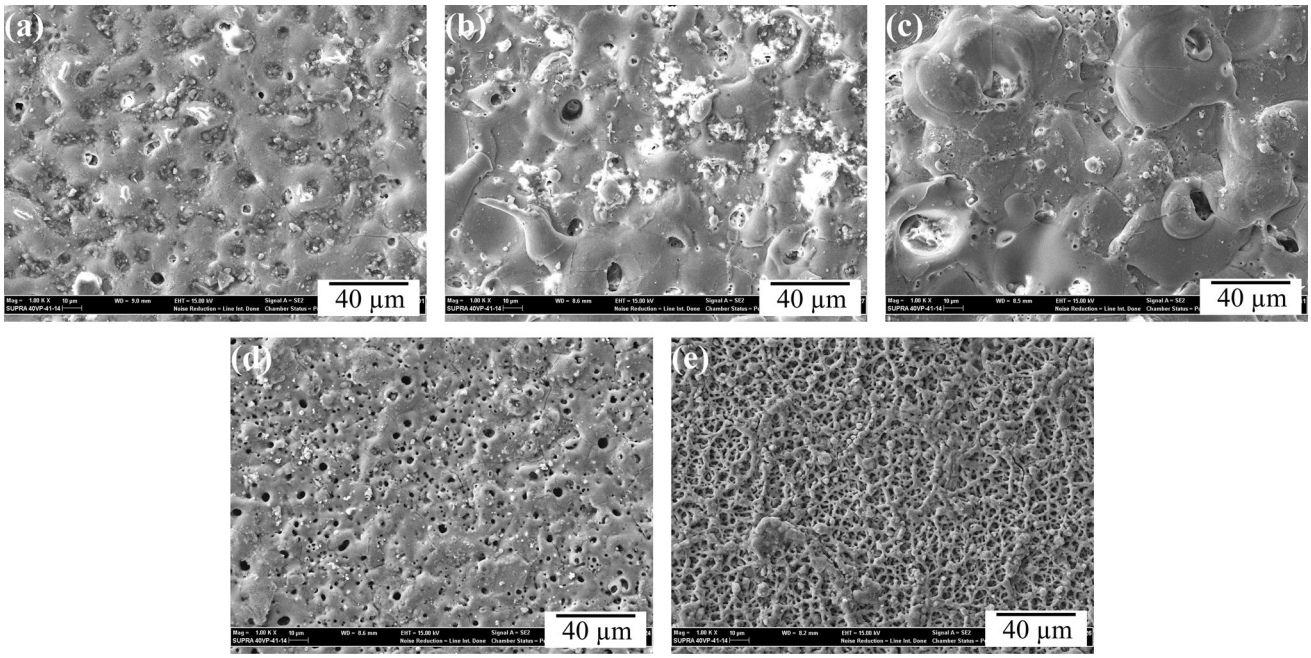


**Fig. 4** Surface SEM micrographs of the MAOed samples (a) A1, (b) A2, (c) A3, (d) B, and (e) C

**Table 4 EDS analyses of the MAO coatings**

| Sample designation | at.% | | | | | | | | |
|---|---|---|---|---|---|---|---|---|---|
| | Mg | O | Si | Zr | Al | P | Na | K | F |
| A1 | 19.79 | 56.94 | 12.71 | 4.03 | 1.31 | … | 4.12 | 0.98 | 1.43 |
| A2 | 23.29 | 57.06 | 12.46 | 4.39 | 1.24 | … | 1.37 | 0.38 | 1.05 |
| A3 | 23.75 | 58.38 | 12.26 | 4.51 | 1.18 | … | 0.62 | 0.29 | 0.19 |
| B | 19.67 | 54.52 | 14.88 | 1.12 | 0.81 | … | 8.24 | 1.57 | … |
| C | 21.11 | 54.82 | … | 5.35 | 8.42 | 3.56 | 4.45 | 1.06 | 1.23 |

contained a slightly higher amount of Zr. Therefore, based on the findings of the EDS analysis, it was seen that $K_2ZrF_6$ addition was more effective than $Na_2ZrO_3$ to incorporate Zr to the MAO coating, and promoted the formation of the $ZrO_2$ phase that is beneficial for its thermal barrier properties. In addition, according to Table 4, aluminum content in sample C was the highest due to its electrolyte containing $NaAlO_2$ compound. However, trace amount of aluminum in the other samples came from the aluminum content (~9 wt. %) in AZ91 alloy, and this suggests that contribution of the alloy's chemical composition to the incorporation of an individual element to the coating may be less than that of the electrolyte.

Cross-sectional SEM micrographs of MAOed samples are shown in Fig. 5. No discontinuity was observed at the interface between the coatings and substrate and all the MAO coatings fabricated in the present study firmly integrated the AZ91 alloy. The coating thickness of samples A1, A2, and A3 (Fig. 5a to c) was well correlated with the applied voltage on those samples and the highest porosity along with large cavities was observed within the coating of sample A3. Since a higher electric field leads to a higher growth rate, thicker coatings were fabricated when a higher voltage was applied (Ref 24). However, surface roughness, pore size, and inhomogeneity increased when both high discharge density and the applied voltage increased. As already quantified in Table 3, many small-sized micro-pores were visible throughout the coating of sample B (Fig. 5d) which were mostly concentrated at the upper part of the MAO coating. Most MAO coatings showed a relatively flat coating-substrate interface except sample C showing a highly curved interface (Fig. 5e). This might be attributed to the varying growth rate of the coating due to a higher electrolyte conductivity provided by the presence of a higher concentration of ions in the electrolyte (i.e., $AlO_2^-$ and $PO_4^{3-}$ ions). Beside it encouraged the formation of a curved interface for sample C, it also led to the highest coating thickness because of the high final current density (Ref 8) even this sample was oxidized at the lowest applied voltage.

In addition to the surface EDS analysis, cross-sectional elemental distribution in the coatings of sample A3, B, and C was studied by using EDS elemental mapping (Fig. 6). Al, Mg, O, and Zr elements are the most common elements in all coatings. It was demonstrated the presence of aluminum throughout the coatings. When compared to samples A3 and B, which were oxidized in the electrolytes without any aluminum containing compound, it was seen that sample A3 has a higher aluminum signals at its outermost surface than sample B. The main difference between them is that sample A3 was oxidized at a higher applied positive voltage (520 V). It

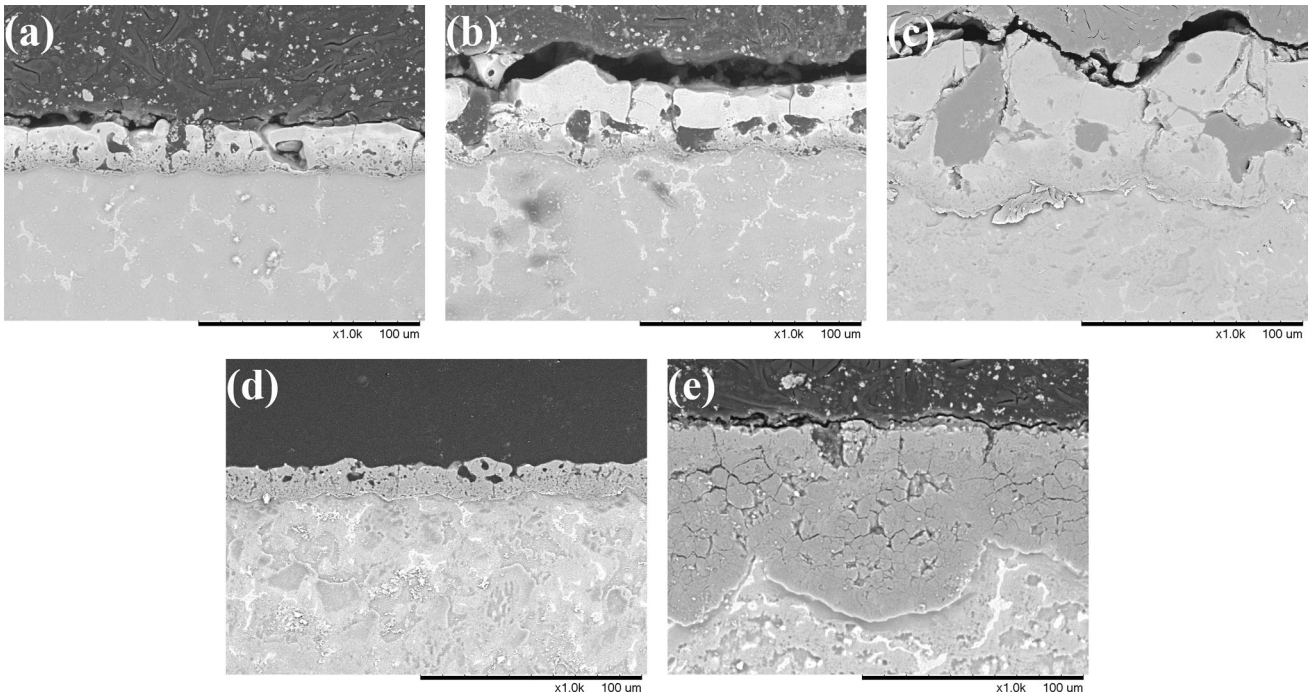


**Fig. 5** Cross-sectional SEM micrographs of the MAOed samples (a) A1, (b) A2, (c) A3, (d) B, and (e) C

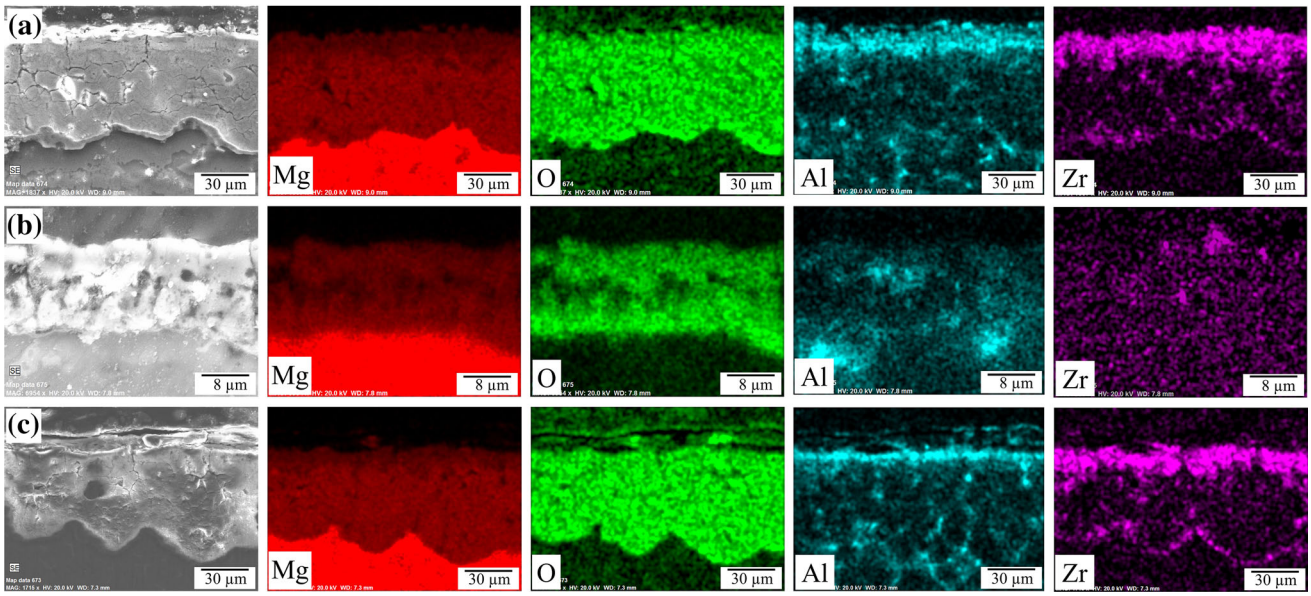


**Fig. 6** EDS elemental mapping of the samples, (a) A3, (b) B, and (c) C

suggests that aluminum atoms coming from the substrate itself can incorporate to the coating structure and concentrate at the outermost surface when a higher positive voltage is applied in the MAO process. In the same manner, sample B indicates a lower amount of aluminum signals at the outermost surface, but more aluminum signals were evident close to the substrate—coating interface for this sample, possibly due to a lower applied positive voltage (400 V). Similarly, aluminum signals in sample C, which was oxidized in $NaAlO_2$ and $Na_3PO_4$ containing electrolyte, concentrate at the outermost surface. This may be attributed to a higher electrical conductivity of its electrolyte despite it was oxidized in a lower applied positive voltage (360 V). Although all samples shown in Fig. 6 indicate aluminum signals on their EDS mapping, it should be kept in mind that EDS mapping gives a relative content in an individual sample, and the highest aluminum content was found in sample C, which was oxidized in an aluminum containing electrolyte, as previously given in Table 4.

It is noticed in Fig. 6 that the amount of Mg element was uniform throughout the cross section, while Zr elements originated from the electrolyte were concentrated at the outermost layer of the coatings. Trace amount of Zr was detected at the innermost layer of the coatings. This is attributed to increment in discharged density at a later stage of the MAO

process promoting more ZrO2 incorporation to the coating (Ref 9). It was also shown that the type of Zr containing compound in the electrolyte may lead to differences in the Zr content in the coatings of the samples oxidized in the same applied voltage. In this context, sample B which was oxidized in the electrolyte containing $Na_2ZrO_3$ (Fig. 6b) contained less amount of Zr (0.81 at.%) than that of sample C (5.35 at.%) which was oxidized in $K_2ZrF_6$ containing electrolyte (Fig. 6a and c).

### 3.4 Phase Analyses in the MAO Coatings

XRD analyses indicated that the MAO coatings formed in the silicate-based electrolyte are composed predominantly of MgO and $Mg_2SiO_4$ as presented in Fig. 7. Additionally, t-$ZrO_2$ phase (high-temperature form of $ZrO_2$) was identified for samples A1, A2, and A3. On the other hand, a dual electrolyte (aluminate—and phosphate-based) was used for sample C, and both MgO and $MgAl_2O_4$ phases were identified for this sample. However, unlike in other MAOed samples, the $ZrO_2$ phase did not appear in the XRD pattern of samples B and C, most probably due to the amorphous nature of Zr containing phases (Ref 2). XRD patterns of all the MAOed samples contained additional strong peaks originating from the Mg substrate such as α-Mg and $Mg_{17}Al_{12}$ due to the penetration of x-rays into the substrate. It should also be noted that any phase containing sodium, potassium, or fluorine was not detected due to their low contents or amorphous nature in the fabricated MAO coatings.

A number of simultaneous reaction takes place during the MAO process. These reactions vary depending on substrate material and electrolyte composition. The phases formed on an Mg-based substrate during the MAO process in silicate-based electrolytes were given in Reactions 3 to 7 (Ref 25).

$$Mg \rightarrow Mg^{2+} + 2e^- \quad \text{(Eq 3)}$$

$$Mg^{2+} + 2(OH)^- \rightarrow Mg(OH)_2 \rightarrow MgO + H_2O \quad \text{(Eq 4)}$$

$$SiO_3^{2-} \rightarrow SiO_2 + 1/2O_2 + 2e^- \quad \text{(Eq 5)}$$

$$2MgO + SiO_2 \rightarrow Mg_2SiO_4 \quad \text{(Eq 6)}$$

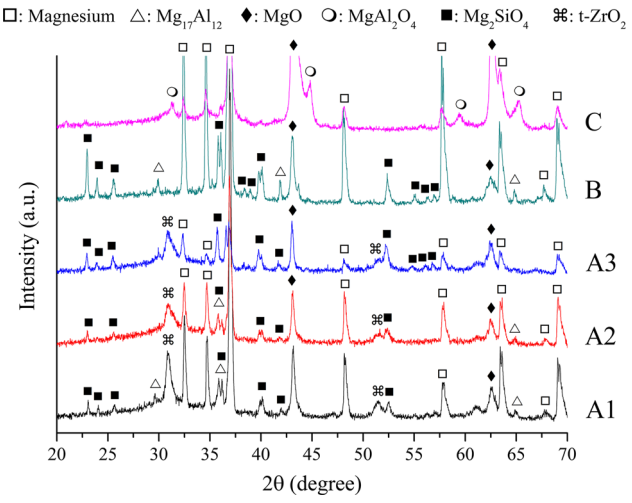


**Fig. 7** XRD patterns of the MAOed samples

$$2Mg^{2+} + 2SiO_3^{2-} \rightarrow Mg_2SiO_4 + SiO_2 \quad \text{(Eq 7)}$$

When Zr containing compounds such as $K_2ZrF_6$ and $Na_2ZrO_3$ are added into the electrolyte, $ZrO_2$ is formed as the product of Reactions 8 to 14 depending on the type of Zr sources (Ref 24, 26, 27).

$$K_2ZrF_6 + 4(OH)^- \rightarrow Zr(OH)_4 + 2K^+ + 6F^- \quad \text{(Eq 8)}$$

$$Zr(OH)_4 \rightarrow ZrO_2 + H_2O \quad \text{(Eq 9)}$$

$$K_2ZrF_6 \rightarrow 2K^+ + ZrF_6^{2-} \quad \text{(Eq 10)}$$

$$ZrF_6^{2-} + 4(OH)^{1-} \rightarrow ZrO_2 + 6F^- + 2H_2O \quad \text{(Eq 11)}$$

$$Na_2ZrO_3 \rightarrow Na_2O + ZrO_2 \quad \text{(Eq 12)}$$

$$Na_2ZrO_3 + 2H_2O \rightarrow ZrO(OH)_2 + 2NaOH \quad \text{(Eq 13)}$$

$$ZrO(OH)_2 \rightarrow ZrO_2 + H_2O \quad \text{(Eq 14)}$$

When the electrolyte composition of sample C was considered, which consists of dual electrolyte composed of $NaAlO_2$ and $Na_3PO_4$, formation of $MgAl_2O_4$ phase is given through Reactions 15 to 20 (Ref 25).

$$AlO_2^- + 2H_2O \rightarrow Al(OH)_4^- \quad \text{(Eq 15)}$$

$$4Al(OH)_4^- - 4e^- \rightarrow 4Al(OH)_3 + 2H_2O + O_2 \quad \text{(Eq 16)}$$

$$2Al(OH)_3 \rightarrow Al_2O_3 + 3H_2O \quad \text{(Eq 17)}$$

$$Mg^{2+} + 2Al(OH)_4^- \rightarrow MgAl_2O_4 + 4H_2O \quad \text{(Eq 18)}$$

$$Al_2O_3 + MgO \rightarrow MgAl_2O_4 \quad \text{(Eq 19)}$$

$$Mg^{2+} + 2Al_2O_3 + 2OH^- \rightarrow MgAl_2O_4 + H_2O \quad \text{(Eq 20)}$$

### 3.5 Microhardness Measurements

The results of the microhardness measurements of the AZ91 alloy and the MAO coatings are shown in Fig. 8. The surface hardness of the bare AZ91 alloy increased 4 to 7 times by the application of the MAO process, and this can be attributed to the formation of hard oxide-based phases during MAO such as $MgAl_2O_4$, $Mg_2SiO_4$, and MgO. Beside the phases formed from the ions of the substrate and the electrolyte, the addition of a Zr-based compound in the electrolyte can also contribute to the hardness of the MAO coating as $ZrO_2$ (6.5 Mohs), which has a higher hardness than MgO. Specifically, the hardness of samples A1, A2, and A3 showed an increasing trend with increasing applied positive voltage and increasing coating thickness.

As presented in Fig. 4 and 5, the surface morphology and cross-sectional microstructure were considerably affected by the applied voltage during the MAO process. The results revealed that decreasing pore fraction due to increasing applied voltage provided a more compact surface morphology and increased hardness. Samples A1 and B, which were both treated in silicate-based electrolytes with different Zr-based com-

pounds, can be comparable in terms of the coating hardness. Because sample A1 and B have approximately 4 and 1 at.% Zr, respectively, the minor difference in their hardness can be attributed to the difference of Zr contents in their coatings.

### 3.6 Pull-Off Tests

Stereo microscope images of the MAOed samples after the pull-off tests are presented in Fig. 9. It was observed that all MAO coatings failed between their loose outer layer and the well-adhered inner barrier layer. This observation was compatible with the presence of the well adhered and discontinuity-free coating-substrate interfaces of the MAO coatings presented in Fig. 5, and therefore, the failure mode was assigned as the cohesive failure rather than the adhesive failure in the pull-off tests. In order to evaluate the cohesive strength of the fabricated MAO coatings, the ratio of the maximum load at the time of failure to the cross-sectional area of the sample was calculated for all MAO samples and listed in Table 5. It was shown that the cohesive strength of the MAO coatings can be well correlated with the average pore size and the total pore fraction given in Table 3, i.e., cohesive strength increased with decreasing pore size and increasing pore fraction. In this context, the lowest cohesive strength was obtained from sample A3 which has the largest pore size and the lowest amount of pores, while the highest cohesive strength was obtained from sample C which has the smallest pore size and the highest amount of pores.

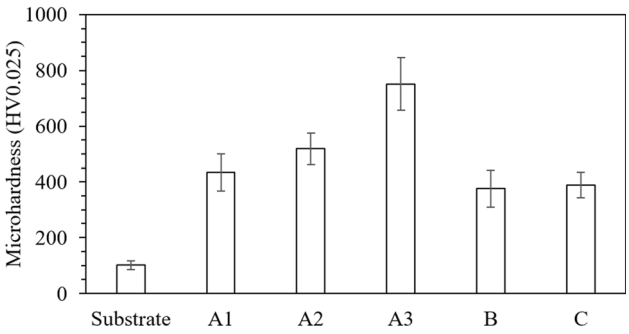


**Fig. 8** Microhardness results of the substrate and the MAOed samples

### 3.7 Thermal Conductivity Tests

Table 6 shows thermal conductivity of the coatings and equivalent thermal conductivity of the samples (substrate + coating) after the MAO process. The results revealed that thermal conductivity of the bare substrate (i.e., AZ91 alloy) was reduced from approximately 7% to 30% by the application of the MAO process in the Zr containing electrolytes. Among all MAOed samples, sample C exhibited the lowest coating thermal conductivity (2.35 W/m.K) and equivalent thermal conductivity (41.89 W/m.K). It was shown that the MAO process is effective to improve thermal insulation properties of AZ91 Mg alloy.

Enhanced insulation capability of the MAO coatings is attributed to low thermal conductivity phases in the coating

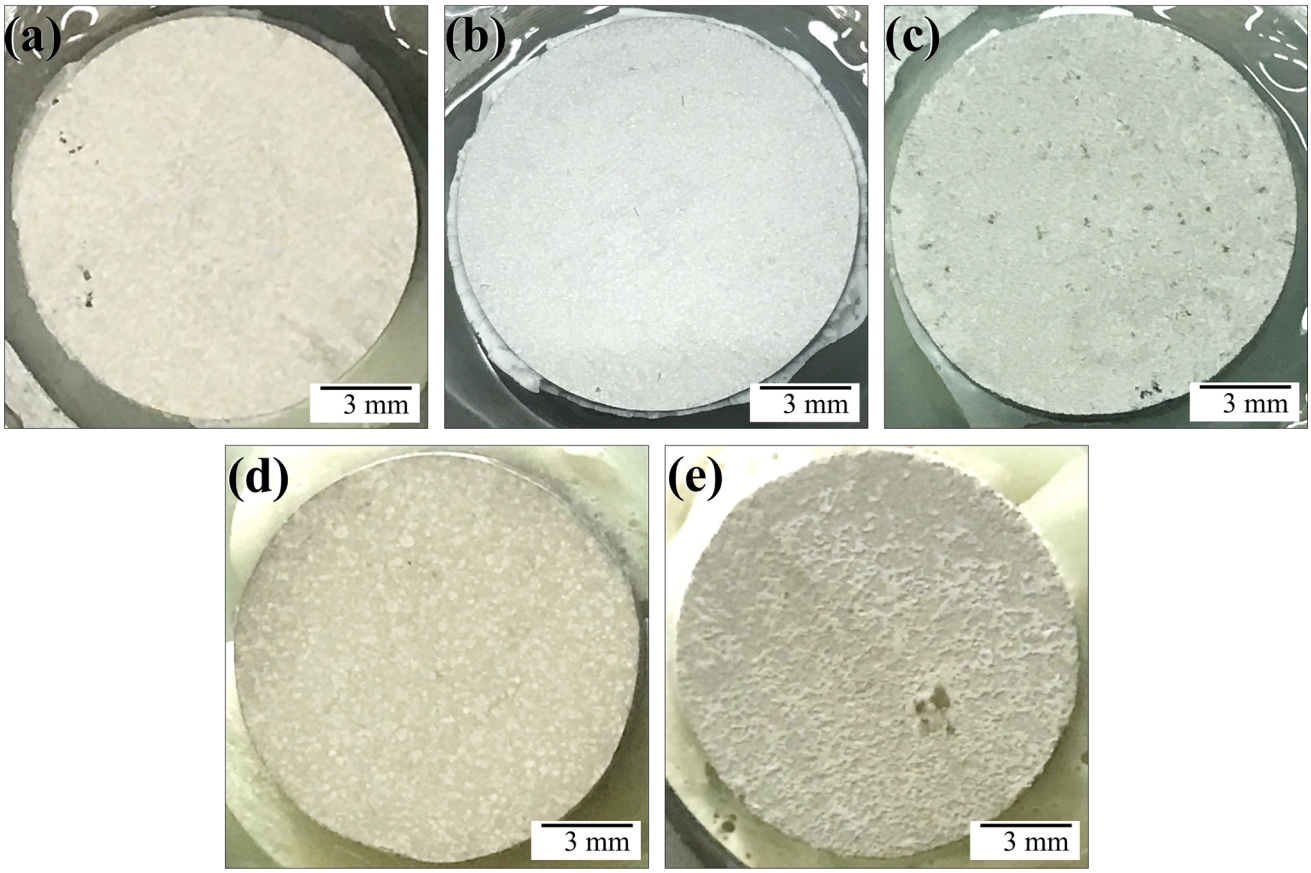


**Fig. 9** Stereo microscope images of the MAOed samples after the pull-off tests (a) A1, (b) A2, (c) A3, (d) B, and (e) C

**Table 5 Cohesive strength values of the MAO coatings**

| Sample designation | Cohesive strength, MPa |
|---|---|
| A1 | 11.9 |
| A2 | 11.8 |
| A3 | 7.5 |
| B | 24.2 |
| C | 35.5 |

**Table 6 Thermal conductivity values of the bare substrate and MAOed samples**

| Sample designation | Coating thermal conductivity, W/m K | Equivalent thermal conductivity, W/ K |
|---|---|---|
| A1 | 3.32 | 54.59 |
| A2 | 3.01 | 51.91 |
| A3 | 2.43 | 44.11 |
| B | 3.71 | 55.49 |
| C | 2.35 | 41.89 |
| Bare substrate | N/A | 59.65* |

*Thermal conductivity of the bare substrate itself

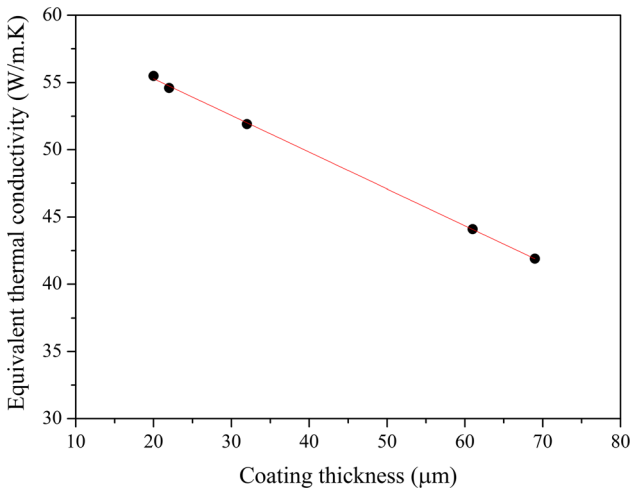


**Fig. 10** Equivalent thermal conductivity vs. coating thickness variation of the MAOed samples

structures. These include t-$ZrO_2$, MgO, $Mg_2SiO_4$, and $MgAl_2O_4$, which were successfully formed to improve the thermal insulation capability of the MAO coatings. Besides the various phases in the coating structure, both surface morphology and coating thickness may have an effect on increased thermal insulation capability of the coating. As presented in Table 3, pore size, pore fraction, and coating thickness widely varied with the electrolyte composition and the applied voltage used in this study. Among these parameters, the coating thickness of the MAOed samples was well correlated with their equivalent thermal conductivities (Fig. 10). For a given electrolyte composition, i.e., the silicate-based electrolyte, samples A1, A2, and A3 showed a decreasing trend for their equivalent thermal conductivity with an increasing order of their coating thickness. Although sample B was oxidized in the silicate-based electrolyte with a different Zr-based addition, it also presented a similar equivalent thermal conductivity to that of sample A1. Similarly, regardless of the differences in their morphological features, samples A3 and C exhibited relatively close equivalent thermal conductivities. It has been previously reported that smaller pores ($< 2$ $\mu$m) decrease the thermal conductivity of porous alumina ceramics, while larger ones ($>14$ $\mu$m) increases (Ref 28). However, it was shown in this study that the pore size in the range of approximately 1 to 6 $\mu$m, and the total pore fraction in the range of approximately 3 to 25 % did not have a remarkable effect on the thermal conductivity. Since A3 and C have approximately same thickness, their thermal conductivities are nearly equal despite the difference in their pore fractions were quite high (~3% and ~25%). The present results showed that coating thickness has more significant effect on the thermal conductivity of MAO coatings than the surface morphology, and the equivalent thermal conductivity is mainly controlled by the coating thickness because of the restriction of the mean free path of the phonon and the enhancement of the phonon scattering process (Ref 9).

### 3.8 Thermal Shock Tests

Surface SEM micrographs of MAOed samples after thermal shock tests are presented in Fig. 11. For sample A1 (Fig. 11a), it is evident that the outermost layer was partially delaminated and minor cracks appeared on the MAO coating. Unlike sample A1, both samples A2 and A3 (Fig. 11b and c) suffered wide cracks throughout their MAO coatings after the thermal shock tests. Samples B and C (Fig. 11d and e) did not exhibit delamination or peeling on their surfaces, but a crack network was apparent on their surfaces.

The crack formation is a result of a thermal expansion incompatibility between the substrate and the coating. However, it was observed that the MAO coatings did not flake off or detach from the substrate completely. Therefore, it was revealed that the fabricated coatings were well adhered to the substrate as previously shown by the pull-off tests. Also, some phases such as MgO, $MgAl_2O_4$, and $ZrO_2$ phases with a high thermal expansion coefficient reduce the thermal expansion incompatibility and prevents the coating detachment from the substrate (Ref 29). It was shown that both the peeling off the top layer of the coating and the crack formation depend on the coating hardness, cohesive strength, and the thermal conductivity of the coatings. Lower hardness, high cohesive strength, and low thermal conductivity are beneficial to increase thermal shock resistance of the coating.

It can be noticed from Fig. 11 that MAO coating of sample A1 showed relatively very low peel off while that of sample A3 showed an almost complete peel off from the loose outer layer. Even though sample A3 had a lower thermal conductivity than samples A1 and A2, the MAO coating of sample A3 had both the highest hardness and lowest cohesive strength, which hampered the thermal shock resistance because it reduced the resistance to thermal strains. Both the partial fragmentation of the outer layer of samples A1 and A2 and the more severe fragmentation of sample A3 were compatible with their corresponding coating thickness and cohesive strength given in Tables 3 and 5, respectively. This correlation showed that the MAO coating, i.e., that of sample A3, with a higher hardness and a lower cohesive strength encouraged the formation of wider cracks and surface fragmentation. On the other hand, the propagation rate of cracks is mainly dependent on the

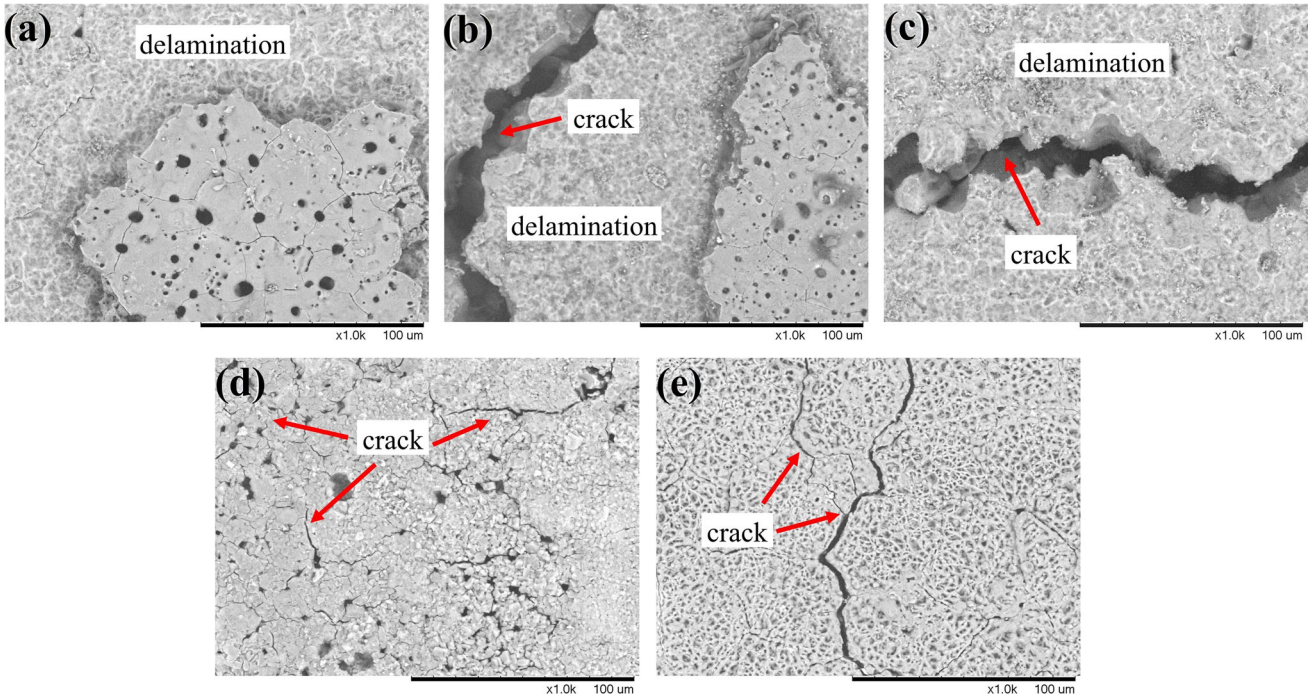


**Fig. 11** Surface SEM micrographs of the MAOed samples (a) A1, (b) A2, (c) A3, (d) B, and (e) C after water-quenched thermal shock tests

toughness of the materials, meaning that a lower toughness and higher induced heat input during the MAO process increased the residual stress in the MAO coating and contributed to the deterioration of sample A3 in the thermal shock test (Ref 30).

Samples B and C exhibited a relatively higher cohesive strength and lower hardness compared to samples A1, A2, and A3. Hence, it is notable that the resistance to delamination and peeling was significantly enhanced for samples B and C. In particular, sample C showed almost the same surface morphology before and after the thermal shock test and thus showed the highest thermal shock resistance owing to the highest pore fraction on the surface (24.8%), the high cohesive strength (35.5 MPa), low hardness (397 HV0.025), and the lowest thermal conductivity (41.89 W/m K).

## 4. Conclusions

Structural and morphological features, hardness, cohesive strength, and thermal resistances of MAO coatings fabricated on AZ91 Mg alloy in different electrolytes with additions of Zr containing compounds (i.e., $K_2ZrF_6$ and $Na_2ZrO_3$) were studied in the present study. The following conclusions were drawn:

1. Incorporation of $ZrO_2$ in the form of tetragonal structure (t-$ZrO_2$) was successfully achieved for samples oxidized in silicate-based electrolytes with $K_2ZrF_6$ addition as the Zr source.
2. Coating thickness, mean surface roughness, and average pore size increased when the applied positive voltage was increased, and there was a corresponding reduction in the pore fraction for samples A1, A2, and A3. The electrolyte with the highest electrical conductivity (45.2 mS/cm) produced thicker and denser MAO coating (i.e., sample C).
3. The cohesive strength of the MAO coatings was well correlated with their corresponding average pore size and total pore fraction, and hence, samples with smaller pore size and higher pore fraction exhibited a higher cohesive strength.
4. The main factors determining the thermal shock resistance of the samples in this study were hardness and cohesive strength of the MAO coatings. Relatively lower hardness and higher cohesive strength of the MAO coatings (i.e., samples B and C) showed higher thermal shock resistance and resulted in a reduced surface fragmentation and inhibition of wider cracks.
5. MAO coating synthesized in a dual electrolyte (aluminate—and phosphate—based) with the addition of $K_2ZrF_6$ as the Zr source showed the best thermal performance due to its low hardness, high cohesive strength, and low thermal conductivity.

### Acknowledgments

The authors greatly acknowledge Dr. H. Mindivan from Bilecik Seyh Edebali University Central Research Laboratory for his support during SEM and EDS analyses. The authors also acknowledge the financial support provided by Istanbul Technical University as a part of the ITU Scientific Research Projects with the Grant No. 39644.

### Author Contributions

ES contributed to investigation, formal analysis, and writing—original draft; FM contributed to investigation, formal analysis, and writing—review and editing; YY contributed to

investigation; ASV contributed to resources; MB contributed to conceptualization, methodology, and writing—review and editing

## References


1. X. Fan, Y. Wang, B. Zou, L. Gu, W. Huang and X. Cao, Preparation and Corrosion Resistance of MAO/Ni-P Composite Coat on Mg Alloy, *Appl. Surf. Sci.*, 2013, **277**, p 272–280. https://doi.org/10.1016/j.apsusc.2013.04.044
2. Z.U. Rehman, S.H. Shin, H.T. Lim and B.H. Koo, Transformation of Plasma Electrolytic Oxidation Coatings from Crater to Cluster-Based Structure with Increase in DC Voltage and the Role of ZrO2 Nanoparticles, *Surf. Coat. Technol.*, 2017, **311**, p 383–390. https://doi.org/10.1016/j.surfcoat.2016.12.112
3. M.J. Wang, C.F. Li and S.K. Yen, Electrolytic MgO/ZrO2 Duplex-Layer Coating on AZ91D Magnesium Alloy for Corrosion Resistance, *Corros. Sci.*, 2013, **76**, p 142–153. https://doi.org/10.1016/j.corsci.2013.06.037
4. S. Lee, H.J. Ham, S.Y. Kwon, S.W. Kim and C.M. Suh, Thermal Conductivity of Magnesium Alloys in the Temperature Range From −125 C to 400 C, *Int. J. Thermophys.*, 2013, **34**, p 2343–2350. https://doi.org/10.1007/s10765-011-1145-1
5. A.A. Luo, Magnesium Casting Technology for Structural Applications, *J. Magn. Alloys*, 2013, **1**, p 2–22. https://doi.org/10.1016/j.jma.2013.02.002
6. A. Srinivasan, J. Swaminathan, M.K. Gunjan, U.T.S. Pillai and B.C. Pai, Effect of Intermetallic Phases on the Creep Behavior of AZ91 Magnesium Alloy, *Mater. Sci. Eng., A*, 2010, **527**, p 1395–1403. https://doi.org/10.1016/j.msea.2009.10.008
7. G.B. Darband, M. Aliofkhazraei, P. Hamghalam and N. Valizade, Plasma Electrolytic Oxidation of Magnesium and its Alloys: Mechanism, Properties and Applications, *J. Magn. Alloys*, 2017, **5**, p 74–132. https://doi.org/10.1016/j.jma.2017.02.004
8. F. Muhaffel and H. Cimenoglu, Development of Corrosion and Wear Resistant Micro-Arc Oxidation Coating on a Magnesium Alloy, *Surf. Coat. Technol.*, 2019, **357**, p 822–832. https://doi.org/10.1016/j.surfcoat.2018.10.089
9. P. Wang, J. Li, Y. Guo, J. Wang, Z. Yang and M. Liang, Effect of Zirconia Sol on the Microstructures and Thermal-Protective Properties of PEO Coating on a Cast Al-12Si Piston Alloy, *J. Alloy. Compd.*, 2016, **657**, p 703–710. https://doi.org/10.1016/j.jallcom.2015.10.139
10. X. Shen, X. Nie, H. Hu and J. Tjong, Effects of Coating Thickness on Thermal Conductivities of Alumina Coatings and Alumina/Aluminum Hybrid Materials Prepared Using Plasma Electrolytic Oxidation, *Surf. Coat. Technol.*, 2012, **207**, p 96–101. https://doi.org/10.1016/j.surfcoat.2012.06.009
11. K.M. Doleker, Y. Ozgurluk, H. Ahlatci and A.C. Karaoglanli, Evaluation of Oxidation and Thermal Cyclic Behavior of YSZ, Gd2Zr2O7 and YSZ/Gd2Zr2O7 TBCs, *Surf. Coat. Technol.*, 2019, **371**, p 262–275. https://doi.org/10.1016/j.surfcoat.2018.11.055
12. C. Wang, J. Hao, Y. Xing, C. Guo and H. Chen, High Temperature Oxidation Behavior of TiO2+ZrO2 Composite Ceramic Coatings Prepared by Microarc Oxidation on Ti6Al4V Alloy, *Surf. Coat. Technol.*, 2015, **261**, p 201–207. https://doi.org/10.1016/j.surfcoat.2014.11.031
13. H. Li, Y. Sun and J. Zhang, Effect of ZrO 2 Particle on the Performance of Micro-Arc Oxidation Coatings on Ti6Al4V, *Appl. Surf. Sci.*, 2015, **342**, p 183–190. https://doi.org/10.1016/j.apsusc.2015.03.051
14. T. Akatsu, T. Kato, Y. Shinoda and F. Wakai, Thermal Barrier Coating Made of Porous Zirconium Oxide on a Nickel-Based Single Crystal Superalloy Formed by Plasma Electrolytic Oxidation, *Surf. Coat. Technol.*, 2013, **223**, p 47–51. https://doi.org/10.1016/j.surfcoat.2013.02.026
15. Y. Zhong, L. Shi, M. Li, F. He and X. He, Characterization and Thermal Shock Behavior of Composite Ceramic Coating Doped With $ZrO_2$ Particles on TC4 By Micro-Arc Oxidation, *Appl. Surf. Sci.*, 2014, **311**, p 158–163. https://doi.org/10.1016/j.apsusc.2014.05.031
16. B.L. Krit, R.Z. Wu, N.V. Morozova, I.O. Kondratsky and V.M. Medvetskova, Coating Effect on Thermal-Physical and Corrosion Characteristics of Ultralight Mg-Based Alloy, *IOP Conf. Series Mater. Sci. Eng.*, 2020, **918**, p 012111. https://doi.org/10.1088/1757-899X/918/1/012111
17. J.A. Curran and T.W. Clyne, The Thermal Conductivity of Plasma Electrolytic Oxide Coatings on Aluminium and Magnesium, *Surf. Coat. Technol.*, 2005, **199**, p 177–183. https://doi.org/10.1016/j.surfcoat.2004.11.045
18. H. Luo, Q. Cai, J. He and B. Wei, Preparation and Properties of Composite Ceramic Coating Containing Al2O3-ZrO2-Y2O3 on AZ91D Magnesium Alloy by Plasma Electrolytic Oxidation, *Curr. Appl. Phys.*, 2009, **9**, p 1341–1346. https://doi.org/10.1016/j.cap.2009.02.017
19. S. Wang, X. Liu, X. Yin and N. Du, Surface & Coatings Technology In fl uence of Electrolyte Components on the Microstructure and Growth Mechanism of Plasma Electrolytic Oxidation Coatings on 1060 Aluminum Alloy, *Surf. Coat. Technol.*, 2020, **381**, p 125214. https://doi.org/10.1016/j.surfcoat.2019.125214
20. V. Dehnavi, B.L. Luan, D.W. Shoesmith, X.Y. Liu and S. Rohani, Effect of Duty Cycle and Applied Current Frequency on Plasma Electrolytic Oxidation (PEO) Coating Growth Behavior, *Surf. Coat. Technol.*, 2013, **226**, p 100–107. https://doi.org/10.1016/j.surfcoat.2013.03.041
21. M. Babaei, C. Dehghanian and M. Vanaki, Effect of Additive on Electrochemical Corrosion Properties of Plasma Electrolytic Oxidation Coatings Formed on CP Ti Under Different Processing Frequency, *Appl. Surf. Sci.*, 2015, **357**, p 712–720. https://doi.org/10.1016/j.apsusc.2015.09.059
22. B. Mingo, R. Arrabal, M. Mohedano, Y. Llamazares, E. Matykina, A. Yerokhin and A. Pardo, Influence of Sealing Post-Treatments on the Corrosion Resistance of PEO Coated AZ91 Magnesium Alloy, *Appl. Surf. Sci.*, 2018, **433**, p 653–667. https://doi.org/10.1016/j.apsusc.2017.10.083
23. Z. Shahri, S.R. Allahkaram, R. Soltani and H. Jafari, Optimization of Plasma Electrolyte Oxidation Process Parameters for Corrosion Resistance of Mg Alloy, *J. Magn. Alloys.*, 2018 https://doi.org/10.1016/j.jma.2018.10.001
24. L. An, Y. Ma, Y. Liu, L. Sun, S. Wang and Z. Wang, Effects of Additives, Voltage and their Interactions on PEO Coatings Formed on Magnesium Alloys, *Surf. Coat. Technol.*, 2018, **354**, p 226–235. https://doi.org/10.1016/j.surfcoat.2018.09.026
25. H.N. Vatan, R. Ebrahimi-kahrizsangi and M. Kasiri-asgarani, Structural, Tribological and Electrochemical Behavior of SiC Nanocomposite Oxide Coatings Fabricated by Plasma Electrolytic Oxidation (PEO) on AZ31 Magnesium Alloy, *J. Alloy. Compd.*, 2016, **683**, p 241–255. https://doi.org/10.1016/j.jallcom.2016.05.096
26. Z.U. Rehman, S.H. Shin, I. Hussain and B.H. Koo, Structure and Corrosion Properties of the Two-Step PEO Coatings Formed on AZ91D Mg Alloy in K2ZrF6-Based Electrolyte Solution, *Surf. Coat. Technol.*, 2016, **307**, p 484–490. https://doi.org/10.1016/j.surfcoat.2016.09.030
27. M. Babaei, C. Dehghanian, P. Taheri and M. Babaei, Surface & Coatings Technology Effect of Duty Cycle and Electrolyte Additive on Photocatalytic Performance of $TiO_2$–$ZrO_2$ Composite Layers Prepared on CP Ti by Micro Arc Oxidation Method, *Surf. Coat. Technol.*, 2016, **307**, p 554–564. https://doi.org/10.1016/j.surfcoat.2016.09.050
28. J. Liu, Y. Li, Y. Li, S. Sang and S. Li, Effects of Pore Structure on Thermal Conductivity and Strength of Alumina Porous Ceramics Using Carbon Black as Pore-Forming Agent, *Ceram. Int.*, 2016, **42**, p 8221–8228. https://doi.org/10.1016/j.ceramint.2016.02.032
29. M.A.L. Braulio, M. Rigaud, A. Buhr, C. Parr and V.C. Pandolfelli, Spinel-Containing Alumina-Based Refractory Castables, *Ceram. Int.*, 2011 https://doi.org/10.1016/j.ceramint.2011.03.049
30. L.I.U. Feng, Y.J. Li, J.J. Gu, Q.S. Yan, L.U.O. Qiang and Q.Z. Cai, Preparation and Performance of Coating on Rare-Earth Compounds-Immersed Magnesium Alloy by Micro-Arc Oxidation, *Trans. Nonferr. Metals Soc. China*, 2012, **22**(7), p 1647–1654. https://doi.org/10.1016/S1003-6326(11)61368-X